Advanced Ceramics Progress: Vol. 11, No. 4, (Autumn 2025) 7-20

Materials and Energy Research Center
MERC

Contents lists available at ACERP

Advanced Ceramics Progress

Journal Homepage: www.acerp.ir

Original Research Article

Tribological enhancement of automotive A356 Al-Si alloy using plasma electrolytic oxidation coating reinforced with SiC nanoparticles

Sina Rahimi [a], Benyamin Yarmand [b,*], Alireza Kolahi [c]

[a] *MS Student, Division, Department of Nanotechnology and Advanced Materials, Materials and Energy Research Center, Karaj, Iran.*
[b] *Associate Professor, Department of Nanotechnology and Advanced Materials, Materials and Energy Research Center, Karaj, Iran.*
[c] *Assistant Professor, Department of Nanotechnology and Advanced Materials, Materials and Energy Research Center, Karaj, Iran.*

* Corresponding Author Email: byarmand@merc.ac.ir (B. Yarmand) URL: https://www.acerp.ir/article_246306.html

ARTICLE INFO

Article History:

Received 04 May 2026
Revised form 26 May 2026
Accepted 18 June 2026

Keywords:

Aluminum-silicon Alloy
SiC Nanoparticles
Plasma Electrolytic Oxidation
Tribological Behavior

ABSTRACT

The poor tribological behavior of the A356 aluminum-silicon alloy remains a significant drawback that limits its use in automotive components. This study aims to improve the surface properties of the A356 alloy through the plasma electrolytic oxidation (PEO) method and to investigate how the incorporation of silicon carbide (SiC) nanoparticles affects its tribological performance. To this end, oxide coatings were prepared on an A356 substrate by the PEO process in silicate electrolytes containing 0 to 2 $g \cdot L^{-1}$ SiC nanoparticles. The results revealed that the incorporation of SiC nanoparticles into the PEO process enhanced the coating formation voltage, resulting in increased coating thickness and hardness, while reducing surface porosity and roughness. Evaluation of the wear performance showed that the wear rate of the A356 substrate decreased from $2.64 \pm 0.02 \times 10^{-4}$ to $1.39 \pm 0.02 \times 10^{-4}$ $mm^3 \cdot N^{-1} \cdot m^{-1}$ with the formation of a pure oxide coating and reached a minimum of $0.17 \pm 0.01 \times 10^{-4}$ $mm^3 \cdot N^{-1} \cdot m^{-1}$ with the incorporation of the maximum concentration of SiC nanoparticles. The evolution of the friction coefficient indicated that the pure oxide coating generated lower friction forces than the A356 substrate, while oxide coatings formed in electrolytes containing up to 1 $g \cdot L^{-1}$ SiC nanoparticles increased the friction coefficient. Notably, for the oxide coating formed in the electrolyte containing 2 $g \cdot L^{-1}$ SiC nanoparticles, the friction coefficient decreased to its lowest value. This behavior resulted from the effect of SiC nanoparticles in reducing friction forces by changing the wear mechanism from sliding to rolling.

https://doi.org/10.30501/acp.2026.580474.1192

1. INTRODUCTION

Aluminum-silicon casting alloys offer a combination of excellent properties, such as high strength, low weight, castability, fluidity, weldability, and cost-effective manufacturing, making them ideal for automotive applications. The use of aluminum-silicon alloys in automotive components contributes to improved performance by reducing weight, fuel consumption, CO_2 emissions, and the overall carbon footprint. Among these alloys, the hypoeutectic A356 alloy is widely used in automotive engine components with complex geometries, such as engine blocks, cylinder heads, and pistons. Its superior casting characteristics, high thermal conductivity for effective heat dissipation, and suitable corrosion resistance make it a preferred choice for critical

Please cite this article as: Rahimi, S., Yarmand, B., & Kolahi, A. (2025). Tribological enhancement of automotive A356 Al-Si alloy using plasma electrolytic oxidation coating reinforced with SiC nanoparticles. *Advanced Ceramics Progress*, *11*(4), 7-20. https://doi.org/10.30501/acp.2026.580474.1192

automotive applications. However, this alloy requires enhanced surface properties to ensure prolonged durability, especially under the harsh operating conditions of combustion engines. The poor tribological characteristics of this alloy, due to its low hardness and high tendency for adhesion, reduce component service life. Moreover, the corrosion resistance provided by the surface oxide layer alone is insufficient to protect parts exposed to severe environments (Alves et al., 2022; Fernández-López et al., 2024; Javidani & Larouche, 2014; XIE et al., 2017; Zhang & Xu, 2022).

Surface modification processes such as hard anodizing and plasma electrolytic oxidation (PEO) are effective methods for improving the tribological properties of aluminum alloys. The application of hard anodizing to aluminum-silicon alloys is limited because the aluminum-rich and silicon-rich phases exhibit different oxide growth rates, making it challenging to achieve a uniform coating. In comparison, numerous studies have shown that the PEO process can produce uniform coatings with superior properties compared to those obtained by hard anodizing on aluminum-silicon alloys. In the PEO process, the oxide layer forms at higher voltages than in hard anodizing, resulting in a distinct coating formation mechanism. The PEO process provides a durable, uniform, and adherent oxide layer on aluminum alloys, enhancing their ability to withstand high contact stresses in tribological systems (Fernández-López et al., 2021; Gulec et al., 2015; Li et al., 2005; Rahimi et al., 2020; A. Yerokhin & Khan, 2010).

To improve the tribological behavior of PEO coatings, strategies involving the incorporation of anionic agents and nanoparticles into PEO coatings through the electrolyte solution have attracted considerable attention from researchers. The effects of anionic components on the characteristics of PEO coatings formed on A356 alloy in aluminate, silicate, and phosphate electrolytes at different concentrations have been extensively studied (Fattah-alhosseini et al., 2020; Fernández-López et al., 2024; Wang et al., 2019). In contrast, the effect of nanoparticles on the tribological performance of PEO coatings on aluminum-silicon alloys has received limited attention. In this regard, the study by Hu et al. can be cited, in which the authors investigated the effects of zirconia nanoparticles and ammonium metavanadate on the hardness and tribological behavior of PEO coatings formed on the ADC12 aluminum-silicon alloy(Hu & Hsieh, 2014). Polunin et al. reported the effects of titanium carbide nanoparticles on the hardness, elastic modulus, wear resistance, and corrosion protection properties of PEO coatings on A356 alloy (Polunin et al., 2021). In another study, Krishtal et al. incorporated silicon dioxide nanoparticles of two different sizes into PEO-treated A361 alloy and investigated their wear and thermal resistance properties (Krishtal et al., 2022).

Silicon carbide (SiC) can be used as a reinforcement to improve the tribological properties of PEO coatings because of its outstanding hardness, excellent wear resistance, and high-temperature stability, which enables it to withstand the elevated temperatures generated during the PEO process. The beneficial effects of these particles on the characteristics of PEO coatings formed on magnesium and titanium alloys have been reported by various researchers (Lian et al., 2020; Yang & Liu, 2010; Yu et al., 2015). In the field of aluminum alloys, Yang et al. investigated the effect of a specific concentration of SiC particles on the corrosion behavior of PEO coatings formed on 6060 aluminum alloy at different current densities (Yang & Liu, 2010). In another study, Aljohani et al. examined the corrosion behavior of PEO coatings containing a specific concentration of SiC particles formed on AA2014 aluminum alloy under different conditions of frequency, current mode, and duty ratio (Aljohani et al., 2022).

Although previous studies have demonstrated that SiC nanoparticles can improve the tribological performance of plasma electrolytic oxidation (PEO) coatings, a systematic understanding of how their concentration influences the oxide layer formation mechanism on A356 alloy, a widely used automotive material, remains lacking. This study addresses this gap by investigating the effect of varying SiC nanoparticle concentrations on the development of the oxide layer. The primary focus is to elucidate how different concentrations of SiC nanoparticles influence the fundamental formation and growth mechanisms of the ceramic oxide coating. Following the preparation of these composite coatings, their tribological behavior was rigorously characterized to quantitatively assess improvements in wear resistance and friction coefficient, providing critical insight into the optimization of coating parameters for enhanced durability.

2. MATERIALS and METHODS

2.1. Sample and coating preparation

Aluminum-silicon alloy A356, with the chemical composition given in Table 1, was used as the substrate. Disc-shaped samples with a diameter of 50 mm and a thickness of 5 mm were fabricated. They were then sequentially ground using a series of SiC abrasive papers with progressively finer grit sizes from 120 to 2000, washed with ethanol, and dried using an air blower to remove any contamination or dust.

The substrates were coated using the PEO process. The PEO setup consisted of a pulsed direct-current power supply, an electrolyte container, and electrodes. The samples functioned as the anodes and were connected to the positive terminal of the power supply. The cathode consisted of a cylindrical stainless-steel container connected to the negative terminal. To maintain a stable temperature during the process, cold water was circulated through the cathode. In addition, the electrolyte was

stirred using a magnetic stirrer to ensure a uniform temperature and a homogeneous composition. Silicate-based electrolytic solutions, consisting of sodium metasilicate.

TABLE 1. Chemical composition of the aluminum-silicon alloy A356

Element	Cu	Mg	Mn	Si	Fe	Zn	Ti	Al
wt%	0.2	0.25	0.1	6.5	0.2	0.1	0.2	Balance

(Na_2SiO_3, Merck, 99%) and potassium hydroxide (KOH, Merck, 95%) were prepared and used either individually or in combination with varying concentrations of SiC nanoparticles (US Research Nanomaterials). This powder exhibited a purity greater than 99% and consisted of β-SiC nanoparticles with an average particle size ranging from 45 to 65 nm. The samples were prepared in silicate electrolytes containing 0, 0.5, 1, and 2 $g \cdot L^{-1}$ SiC nanoparticles and were designated T0, T0.5, T1, and T2, respectively. The characteristics of the electrolytes and samples are presented in Table 2. The coating process was carried out by applying a current density of 0.1 $A \cdot cm^{-2}$ with a duty cycle of 75% for 30 min. At the end of the coating process, the samples were washed with water and ethanol and then dried by air blowing.

TABLE 2. The sample and electrolyte specifications

Sample	Electrolyte concentration ($g.L^{-1}$)			Conductivity ($mS.cm^{-1}$)	pH
	Na_2SiO_3	KOH	SiC		
T0	40	8	0	31.2	13.5
T0.5	40	8	0.5	29.9	13.6
T1	40	8	1	20.2	13.5
T2	40	8	2	9.5	13.4

2.2. Characterization

Phase identification was conducted using X-ray diffractometry (XRD, Philips PW3710) with Cu Kα radiation at a wavelength of 0.154056 nm. A field-emission scanning electron microscope (FESEM, TESCAN-MIRA3) was utilized in both secondary electron and backscattered electron imaging modes to examine the surface morphology, coating thickness, and cross-sectional uniformity. Moreover, energy-dispersive X-ray spectroscopy (EDS) was employed to analyze the chemical composition and elemental distribution across the surface and thickness of the coatings using a C-MAX spectrometer.

The thickness of the coatings was measured using a Phynix-FN coating thickness gauge equipped with n-type probes. This device operates based on the eddy-current principle to measure the thickness of non-conductive (ceramic) coatings on non-ferrous alloys (aluminum). The reported thickness values represent the average of three independent measurements. The surface roughness of the coatings was measured using a TR100 surface roughness tester. Each reported roughness value represents the average of three measurements.

Micro-indentation was performed on the sample surfaces using a Micro Materials Nanotest 600 instrument equipped with a Berkovich indenter under a load of 2 N. Microhardness was calculated from the load and indentation depth data.

2.3. Wear Test

The wear test was conducted using a pin-on-disk tribometer on both the coated samples and the A356 substrate at room temperature. The experiments were performed in a rotating-disk configuration at a sliding speed of 0.02 $m \cdot s^{-1}$. The tribological behavior of the coatings and the substrate was evaluated under dry sliding conditions against an AISI 52100 steel pin under an applied normal load of 2 N. This load was selected after preliminary testing to ensure that the indentation depth remained below 10–15% of the coating thickness, thereby minimizing substrate influence and enabling measurement of the intrinsic coating hardness. A total sliding distance of 100 m was maintained for all tests. The wear rate (Rw) was determined from the measured weight loss as follows (Sabatini et al., 2010):

$$R_w = {\Delta m}/{\rho LD} \quad (1)$$

where Δm is the material weight loss after wear, ρ represents density, L denotes the applied normal load, and D reflects the sliding distance. Moreover, the wear tracks were analyzed using the FESEM and a surface profilometer (Raga3) to determine the wear mechanisms and the width as well as depth of the wear scars, respectively.

3. RESULTS and DISCUSIONS

3.1. Characterization of SiC nanoparticles

The nanoparticles used in this study were characterized by XRD and FESEM, as shown in Figure 1. Phase identification of the diffraction peaks in the XRD pattern shown in Figure 1a indicates that the peaks appearing at 35.6°, 41.3°, 59.9°, 71.8°, and 75.4° are attributed to the (111), (200), (220), (311), and (222) planes, respectively, of cubic silicon carbide (β-SiC), according to JCPDS card No. 29-1129. The FESEM image shown in Figure 1b confirms that the particle dimensions are within the

nanometer range (Aljohani et al., 2022; Yang & Liu, 2010; Yu et al., 2015).

3.2. Appearance of the samples

The appearance photographs and OM images of the surface and cross-sections of the samples are presented in Figure 2. A homogeneous gray oxide layer formed on the surface of all A356 substrates, resulting in the disappearance of the metallic luster. The OM images reveal the absence of defects such as cracks, fractures, or peeling at the microscopic scale on the surface of the oxide layer. Only dark spots are visible that may be related to coarse surface porosity, which is characteristic of PEO coatings. In the cross-sectional OM images of the substrates, the typical microstructure of hypoeutectic aluminum-silicon casting alloy, including primary aluminum dendrites separated with interdendritic aluminum-silicon eutectic, is observed (Sabatini et al., 2010; XIE et al., 2017). On the A356 substrate, an oxide layer is visible that grows with different thicknesses and a rough surface. No signs of separation can be found at the interface of the oxide layer with the substrate, indicating a strong connection.

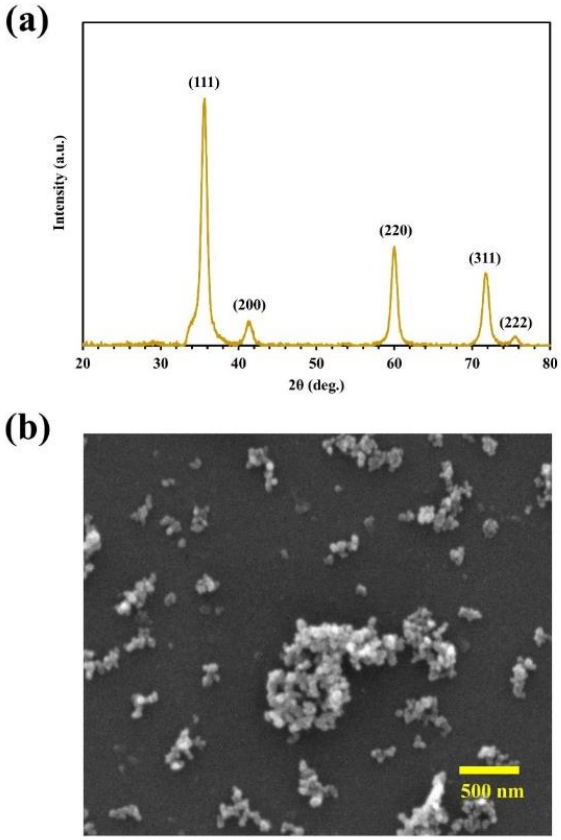

Figure 1. (a) XRD pattern and FESEM image of SiC nanoparticles

3.3. Response voltage changes during oxidation

- The formation of the oxide layer on aluminum-silicon alloy substrates was investigated by monitoring the response voltage at a constant applied current during the process. The response voltage as a function of oxidation time is presented in Figure 3. All curves follow a similar trend, and their evolution can be divided into three stages.

In the first stage, referred to as anodization, the response voltage increases rapidly and reaches values above 350 V after approximately 90 s. These changes indicate the formation of a passive film due to the interaction of aluminum and silicon cations from the A356 substrate with electrolyte anions, accompanied by the emission of small gas bubbles. As the passive film grows and the penetration of oxygen anions through the film becomes increasingly difficult, electrical charges accumulate on the substrate surface, leading to the occurrence of electrical micro-sparks simultaneously with anodization. The onset of this stage, known as spark anodizing, is indicated by a decrease in the slope of the response voltage curve, resulting from electron flow during the overall current cycle. At this stage, electrical micro-sparks appear on the sample surface as tiny white sparks that rapidly spread across the entire surface. The occurrence of these micro-sparks promotes oxide layer growth through the melting and solidification of material in the vicinity of the discharge channels. As the number and intensity of the electrical micro-sparks increase, the oxide layer growth mechanism transitions to micro-arc oxidation (MAO), and the formation of the oxide coating continues in a stable manner. This stage, referred to as MAO, is characterized by a further decrease in the slope of the response voltage curve and the attainment of relative voltage stability (Erfanifar et al., 2017; Hoseini et al., 2021; A. L. Yerokhin et al., 1999).

Comparison of the curves during the anodization stage reveals that the addition of SiC nanoparticles causes a relative increase in the slope of the response voltage-time curve, indicating a change in the nature of passive film formation. Given that the total current at this stage consists exclusively of ionic currents, the increased slope may be attributed to an increase in the electrical resistance of the passive film resulting from the incorporation of SiC nanoparticles. The effect of SiC nanoparticles on increasing the formation voltage persists throughout the process and becomes more pronounced during the MAO stage. At this stage, the electrical resistance of the system depends on both the oxide layer and the electrolyte. The electrical resistance of the oxide layer increases due to compaction resulting from the embedment of SiC nanoparticles, leading to a reduction in the ionic current contribution to the growth mechanism. In addition, the electrolyte conductivity measurements presented in Table 2 indicate an increase in electrolyte resistance in the presence of SiC nanoparticles. Therefore, the increase in the overall electrical resistance of the system causes the response

voltage to rise under a constant applied current and promotes the occurrence of more energetic micro-discharges due to the reduced contribution of ionic current. This change in the oxide layer formation mechanism can be observed through the appearance of stronger electrical micro-sparks on the sample surface (Hoseini & Yarmand, 2020; Matykina et al., 2007; Sharifi et al., 2016).

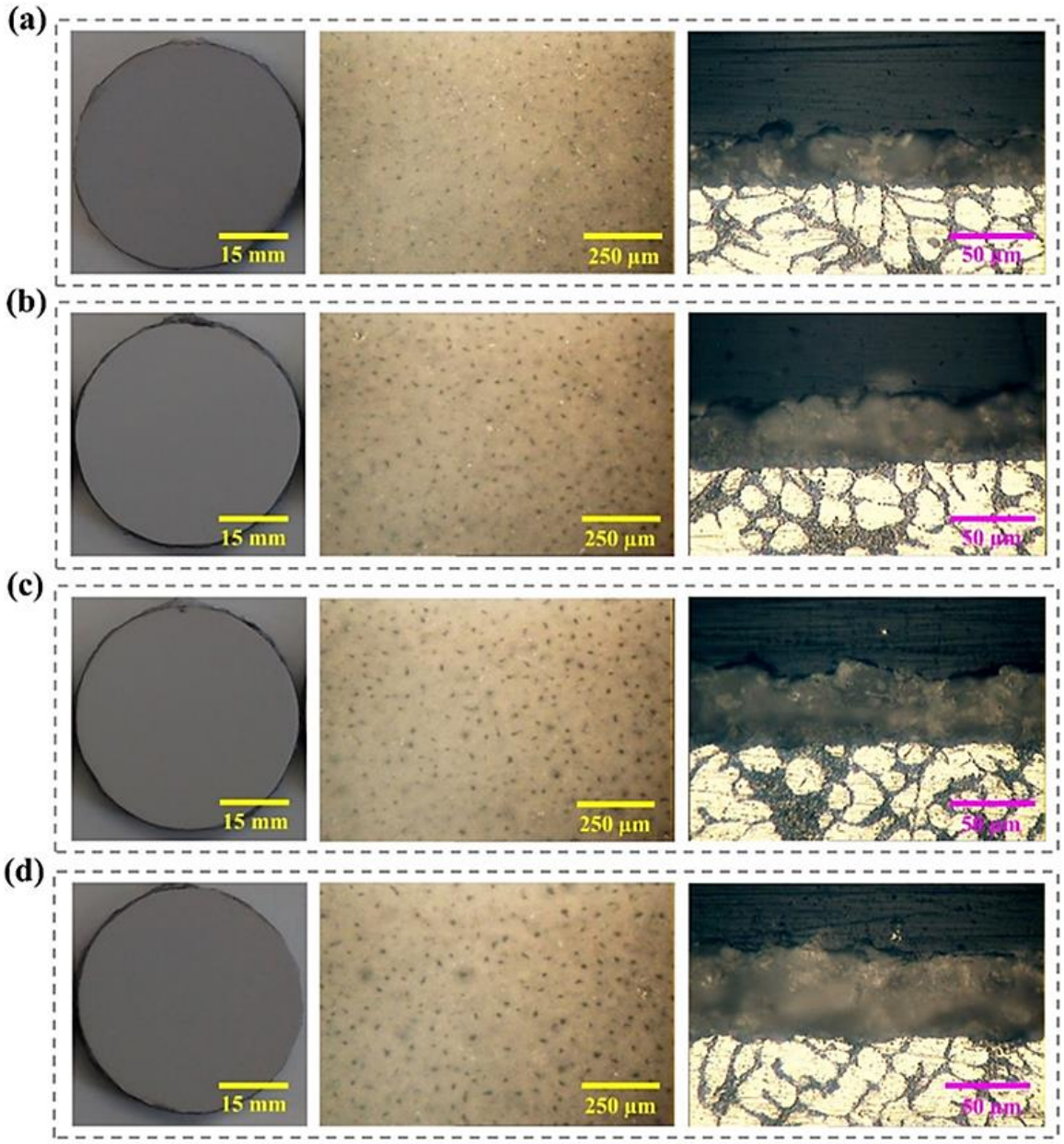

Figure 2. Appearance and OM images from the top and cross-section of (a) T0, (b) T0.5, (c) T1, and (d) T2

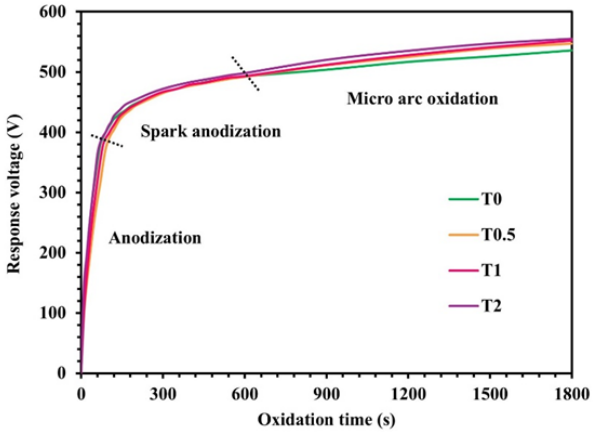

Figure 3. The variations of response voltage versus oxidation time during the PEO process

3.4. Morphology of oxide coatings

FESEM images of the sample surfaces are presented in Figure 4. The morphology resembles resolidified molten oxide with numerous pores distributed across the surface of all oxide layers. This microstructure results from the occurrence of countless electrical micro-sparks on the A356 substrate during the MAO stage. With each micro-spark event, a large number of electrons accumulated on the surface of the oxide layer avalanche through the discharge channel toward the substrate. The intense heat generated along the discharge path causes rapid melting of the channel wall materials. These molten materials are expelled by the pressure of the escaping gases and immediately solidify upon contact with the cold electrolyte. Repeated electrical micro-spark events continuously reshape the solidified material and facilitate gas escape, resulting in the formation of pores of various sizes (Dehnavi et al., 2015; Ebrahimi et al., 2019; A. L. Yerokhin et al., 2000).

The surface porosity of the samples was calculated from binary images obtained from the FESEM micrographs. The total area of black regions within a selected area was considered the relative surface porosity. The relative surface porosity values were 20.9 ± 1.2%, 15.5 ± 0.9%, 12.7 ± 0.8%, and 9.6 ± 0.5% for T0, T0.5, T1, and T2, respectively. This decreasing trend can be attributed to the presence of SiC nanoparticles at the sites of electrical micro-sparks, where they absorb part of the generated heat. As a result, a smaller volume of material melts, leading to the formation of smaller lava features with finer porosity during oxide layer growth. Moreover, the adsorption of SiC nanoparticles into the discharge channels due to electrophoretic forces, together with their filling effect within these channels, can also contribute to the reduction in surface porosity (Hoseini & Yarmand, 2023; Sharifi et al., 2016).

EDS maps of the specimen surfaces, shown in Figure 4, reveal that oxygen is uniformly distributed alongside aluminum and silicon, indicating the formation of an oxide layer with the combined participation of the A356 alloy constituents. Carbon is detected in T0.5, T1, and T2 following the addition of SiC nanoparticles, and its content increases together with that of silicon, confirming the incorporation of SiC nanoparticles into the oxide layer microstructure. The carbon signal corresponds to embedded SiC nanoparticles. The presence of negatively charged SiC nanoparticles during MAO causes them to migrate toward the positively charged substrate under the influence of electrophoretic forces, particularly within discharge channels characterized by high surface energy. As a result, these nanoparticles become entrapped within the molten material during melt ejection and are subsequently incorporated into the oxide layer through repeated electrical micro-spark events.

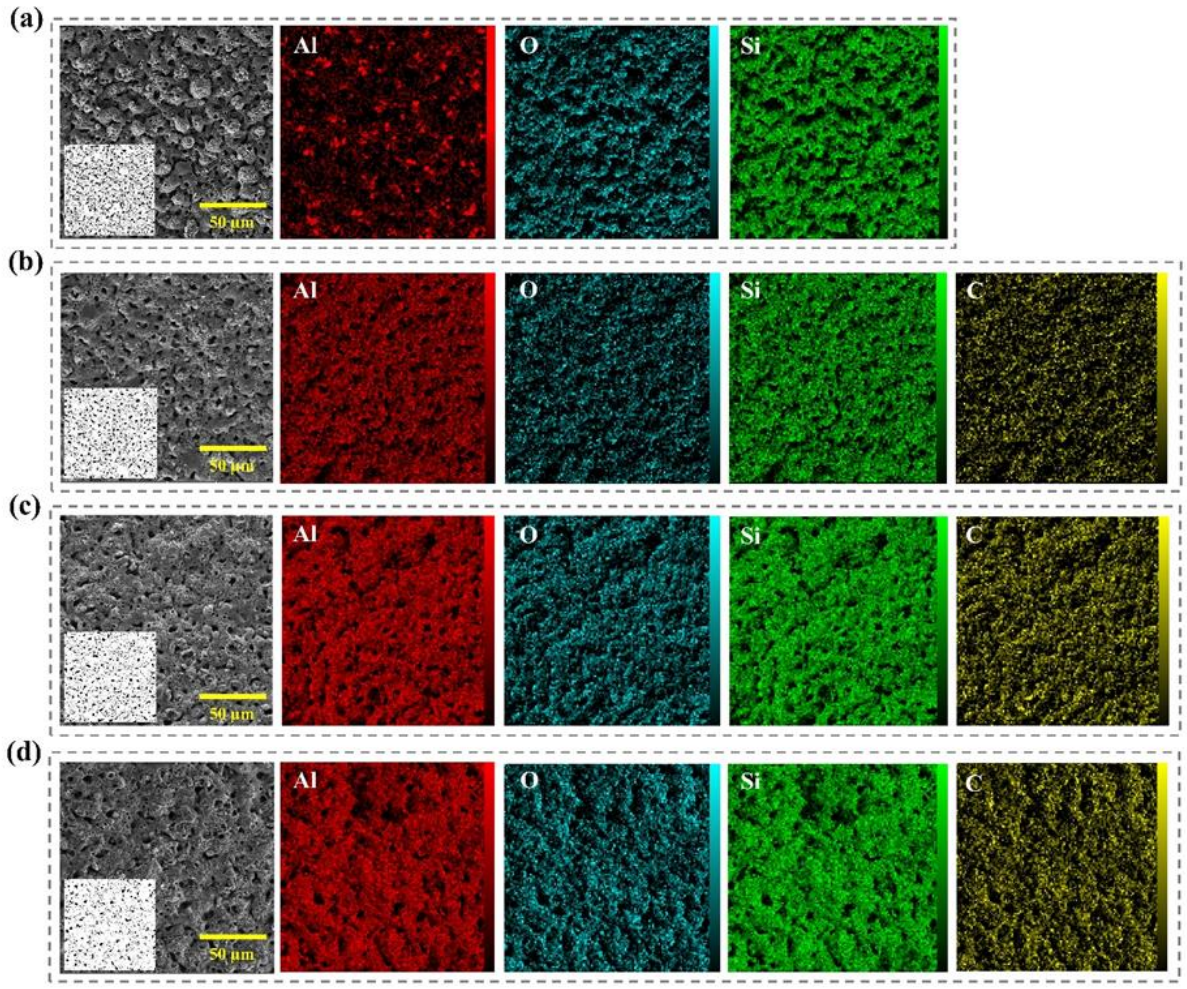

Figure 4. FESEM and binary images along with EDS maps from top of (a) T0, (b) T0.5, (c) T1, and (d) T2

FESEM cross-sectional images of the samples, along with the corresponding EDS maps, are presented in Figure 5. In all samples, the oxide layer grew uniformly on the substrate without cracks or delamination, indicating good adhesion strength. The interface between the oxide layer and the substrate exhibits a wavy morphology, resulting from the non-uniform dissolution of the substrate caused by the presence of silicon in the A356 alloy. This element can locally form oxide compounds with lower melting points than aluminum oxide, leading to localized melting of small regions on the substrate surface. Similar to typical PEO coatings, the microstructure of the oxide layers consists of two distinct regions. First, a thin and dense layer grows directly on the substrate during the initial stage of the process and is referred to as the functional layer. Subsequently, a thicker layer containing more structural defects forms on top of the functional layer under the non-equilibrium conditions of the MAO process and is known as the technological layer. Comparison of the oxide layer thicknesses indicates that the incorporation of SiC nanoparticles into the coating microstructure promotes an increase in coating thickness (Sabatini et al., 2010).

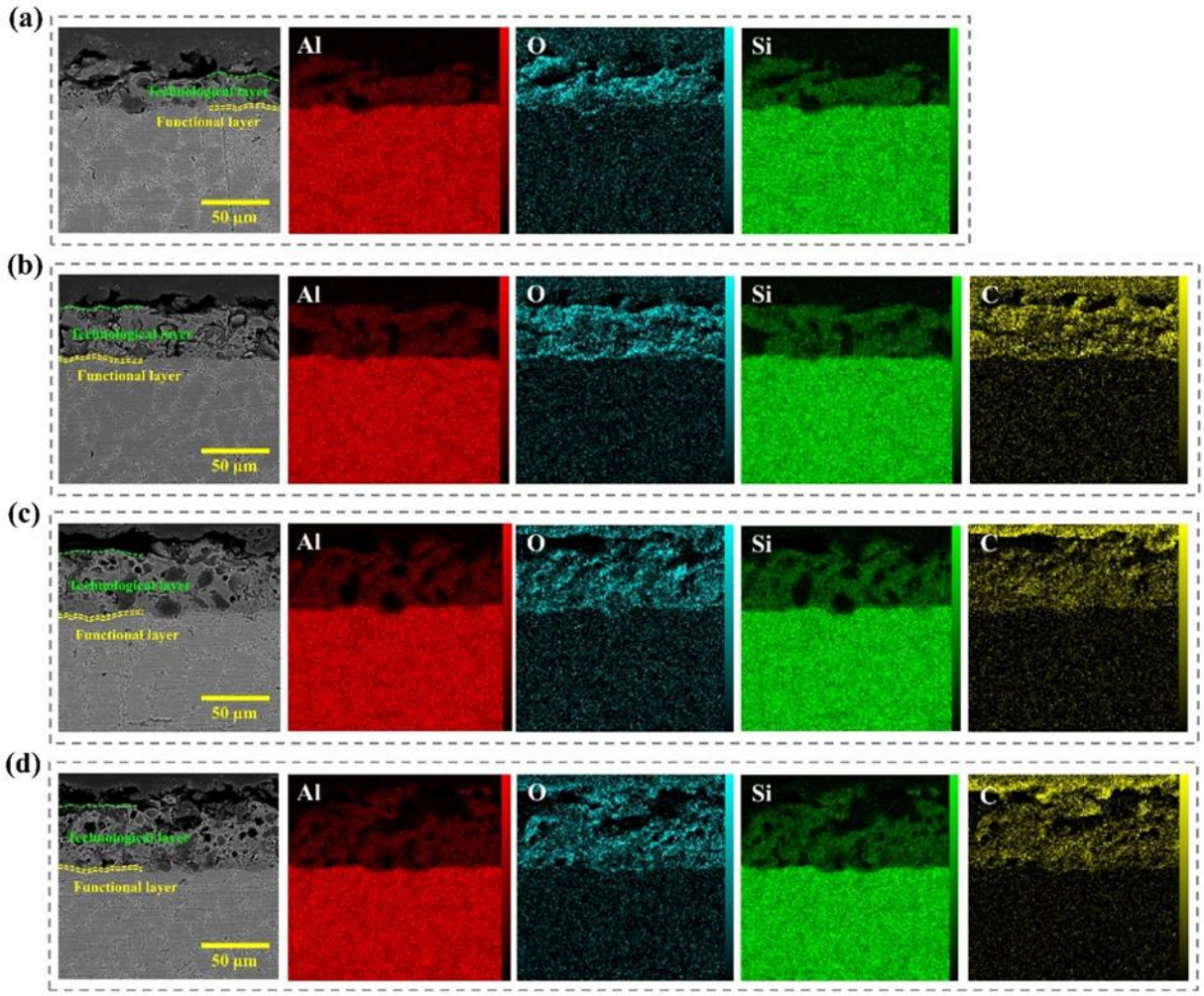

Figure 5. FESEM images along with EDS maps from the cross-section of (a) T0, (b) T0.5, (c) T1, and (d) T2

3.5. Thickness and surface roughness of coatings

The variations in coating thickness and surface roughness are presented in Figure 6. The average thickness of T0 is 33.4 ± 1.4 µm, which increases with the addition of SiC nanoparticles and reaches 50.8 ± 1.1 µm for T2. This increase can be attributed to the competition between oxide layer growth and layer destruction processes. The oxide layer grows through the oxidation of materials during the MAO process and may be partially destroyed as a result of the effects of electrical micro-sparks. Oxide layer growth occurs through the reaction of electrolyte anions with aluminum and silicon cations originating from the A356 substrate. In addition, the melting and transport of material to the surface during electrical micro-spark events contribute to oxide layer development. Conversely, dissolution of the oxide layer or its erosion under the severe conditions generated by electrical micro-sparks can lead to layer degradation.

The increase in coating thickness indicates that the presence of SiC nanoparticles during MAO promotes oxide layer growth and increases the deposition rate by shifting the balance in favor of coating formation processes (Sharifi et al., 2016). The incorporation of SiC nanoparticles during MAO also causes the surface roughness to decrease from 2.52 ± 0.12 µm for T0 to approximately 2 µm for the nanoparticle-containing samples. This effect may be attributed to the absorption of released heat by the SiC nanoparticles, which reduces the volume of molten material and leads to finer surface porosity. Furthermore, the entrapment of SiC nanoparticles within the discharge channels and their filling effect on surface pores reduce the height difference between surface protrusions and depressions, thereby decreasing the overall surface roughness (Hoseini & Yarmand, 2024; Lu et al., 2016; Nasiri Vatan et al., 2016; Sharifi et al., 2016).

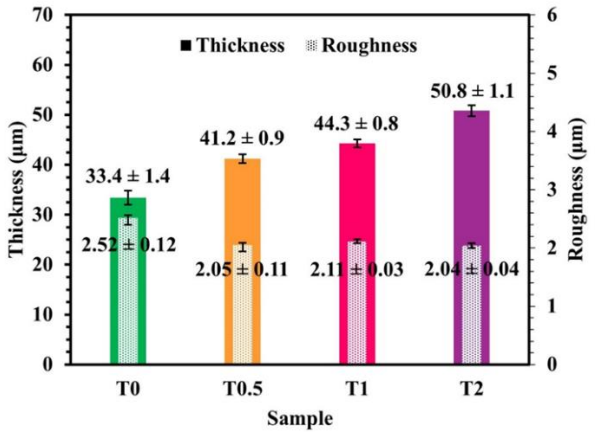

Figure 6. The thickness and roughness variations of the samples

3.6. Identification of crystalline phases

The XRD patterns of the samples at two magnifications are presented in Figure 7. In all patterns, the diffraction peaks located at 38.5°, 44.7°, 65.1°, and 78.3° correspond to the (111), (200), (220), and (311) planes of aluminum, respectively, according to JCPDS card No. 00-004-0787. The peaks appearing at 28.3°, 47.4°, 56.3°, and 70.1° are assigned to the (111), (220), (311), and (400) planes of silicon, respectively, according to JCPDS card No. 00-027-1402. The appearance of these peaks may result from the penetration of X-rays through the oxide coating and into the substrate. The intensity of these peaks decreases with increasing SiC nanoparticle concentration, which can be attributed to the increased thickness of the oxide coating.

The peaks centered at 46.1° and 67.2° are attributed to the (400) and (440) planes of γ-Al_2O_3, respectively, according to JCPDS card No. 00-029-0063. This finding confirms that oxidation of the A356 substrate occurred successfully and that the desired oxide coating was formed. Considering the thickness of the oxide layer, the relatively low intensity of these peaks may be attributed to the predominantly amorphous structure of the grown oxides. Notably, peaks associated with crystalline silica were not detected in the patterns, which may be due to its low content or amorphous nature. Moreover, α-Al_2O_3 was not formed in the oxide coating because the temperature required for the transformation of γ-Al_2O_3 to α-Al_2O_3 was not achieved. Since the presence of silicon in the A356 alloy can absorb part of the heat generated by electrical micro-sparks, it may hinder the transformation or crystallization of amorphous phases.

With increasing SiC nanoparticle concentration in the electrolyte, characteristic SiC peaks appear at 35.6°, 59.9°, and 71.8°, corresponding to the (111), (220), and (311) planes, respectively, according to JCPDS card No. 29-1129 (Figure 7b). These peaks become more pronounced in T2, which contains the highest concentration of SiC nanoparticles. The presence of these diffraction peaks confirms the successful formation of the composite coating (Aljohani et al., 2022; Nasiri Vatan et al., 2016; Sharifi et al., 2016; Yang & Liu, 2010).

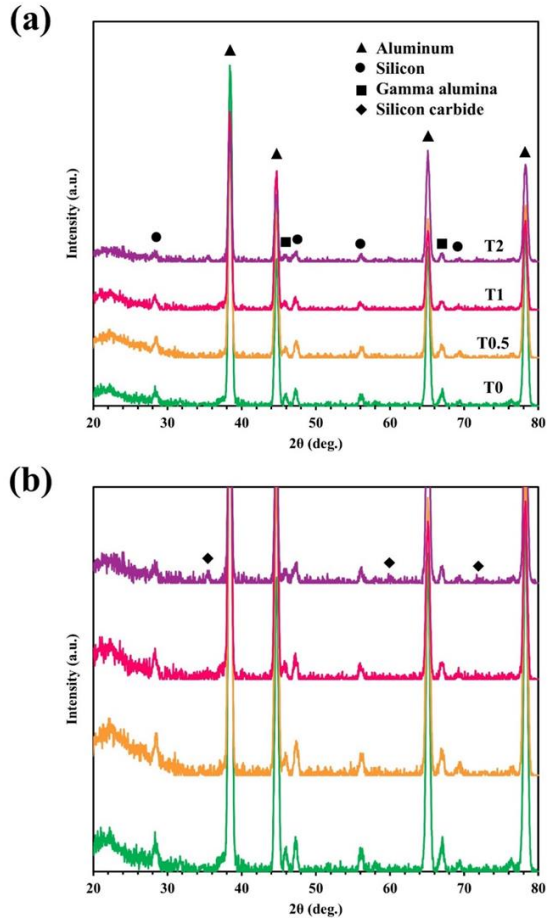

Figure 7. XRD patterns of the samples at two magnifications

3.7. Hardness of oxide coatings

The hardness values of the coatings, together with that of the A356 substrate for comparison, are presented in Figure 8. T0 exhibits a hardness of 498 ± 2 HV, which is approximately six times higher than that of the substrate (73 ± 1 HV). This increase is attributed to the ceramic nature of the oxide coating formed by the PEO process. With the incorporation of SiC nanoparticles, the hardness of the coatings increases further and reaches a maximum value of 946 ± 3 HV for T2. This upward trend results from the high hardness of the SiC nanoparticles, which reinforce the composite oxide layer after being embedded within its microstructure. Furthermore, the participation of these nanoparticles in the coating formation process, together with their incorporation into the inherent defects of the PEO coating, leads to a more compact coating structure, consistent with the surface porosity and roughness results presented in Sections 3.4 and 3.5 (Nasiri Vatan et al., 2016; Sabatini et al., 2010).

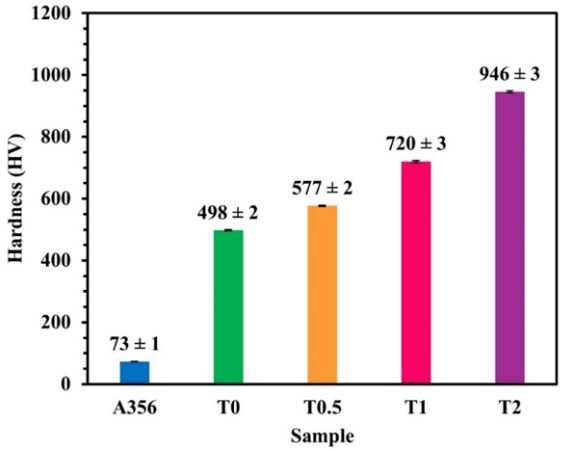

Figure 8. The hardness variations of the samples

3.8. Tribological behavior of oxide coatings

The evolution of the friction coefficient as a function of sliding distance for the samples and the A356 substrate is presented in Figure 9. The friction coefficient of the A356 substrate increases at the beginning of the sliding motion and reaches a maximum value of approximately 1. It then stabilizes at about 0.6 after a sliding distance of 50 m. The initial increase is attributed to the plowing of the substrate surface asperities by the AISI 52100 steel pin, generating high frictional forces. At this stage, the contact surfaces are exposed through the removal of asperities and contaminants. Simultaneously, the interaction between the pin and the A356 substrate under dry sliding conditions causes the amount of debris generated between the sliding surfaces to increase rapidly, enhancing adhesion and resulting in a higher friction coefficient. After approximately 50 m, a dynamic equilibrium is established between the particles entering and leaving the contact region, leading to a stable friction coefficient.

The friction coefficient of T0 is more stable throughout the sliding distance and exhibits an average value of approximately 0.4. Compared with the A356 substrate, this behavior is attributed to the ceramic nature of the oxide coating, which alters the interaction with the steel pin. The tribological behavior of this sample is synergistically influenced by the surface morphology, roughness, and hardness of the oxide coating formed by the PEO process. The friction coefficients of T0.5 and T1 increase relative to T0 and, after exhibiting fluctuations during the first half of the sliding distance, stabilize at an average value of approximately 0.9. This increase may be attributed to the incorporation of hard SiC nanoparticles into the composite oxide layer, which enhances the friction coefficient. The frictional behavior is also influenced by the microstructural compactness, surface porosity, and roughness of the oxide coatings. In contrast, the friction coefficient of T2 initially increases and then becomes nearly constant at approximately 0.5 after 60 m of sliding. This reduction may result from the rolling effect generated by the higher concentration of SiC nanoparticles on the contact surfaces compared with the other samples, causing them to act as solid lubricants during the sliding experiment (Nasiri Vatan et al., 2016; Sharifi et al., 2016; Yu et al., 2015).

The wear rates and wear track profiles of the samples, together with those of the A356 substrate, are shown in Figure 10. The A356 substrate exhibits the highest wear rate, $2.64 \pm 0.02 \times 10^{-4}$ $mm^3 \cdot N^{-1} \cdot m^{-1}$, which decreases markedly to $1.39 \pm 0.02 \times 10^{-4}$ $mm^3 \cdot N^{-1} \cdot m^{-1}$ for T0 following the formation of the oxide layer. With the incorporation of SiC nanoparticles into the microstructure of the oxide coatings, the wear rate decreases significantly and reaches a minimum value of $0.17 \pm 0.01 \times 10^{-4}$ $mm^3 \cdot N^{-1} \cdot m^{-1}$ for T2. As shown in Figures 10b and 10c, the wear track of the A356 substrate exhibits the greatest width and depth, both of which decrease following the formation of the oxide coating. Subsequently, these values continue to decrease with the incorporation of SiC nanoparticles and reach their minimum values in T2.

In general, the tribological behavior of materials is strongly influenced by their mechanical properties. Therefore, the reduction in wear rate can be attributed primarily to the increase in coating hardness, in accordance with Archard's law. The formation of the oxide layer substantially increases the surface hardness of the A356 substrate, while the incorporation of SiC nanoparticles further enhances hardness through reinforcement of the composite microstructure. This factor, together with the increased compactness and the reduced surface porosity and roughness of the oxide layers, improves the wear resistance of the coating and decreases material loss. Moreover, the high concentration of SiC nanoparticles in the reinforced coatings can alter the wear mechanism from sliding to rolling by becoming positioned between the contact surfaces. These nanoparticles act as microscopic rolling elements within the contact region, thereby transforming the frictional interaction from sliding to rolling. Consequently, both the friction coefficient and wear rate decrease, as observed for T2 (Nasiri Vatan et al., 2016; Sharifi et al., 2016; Yu et al., 2015).

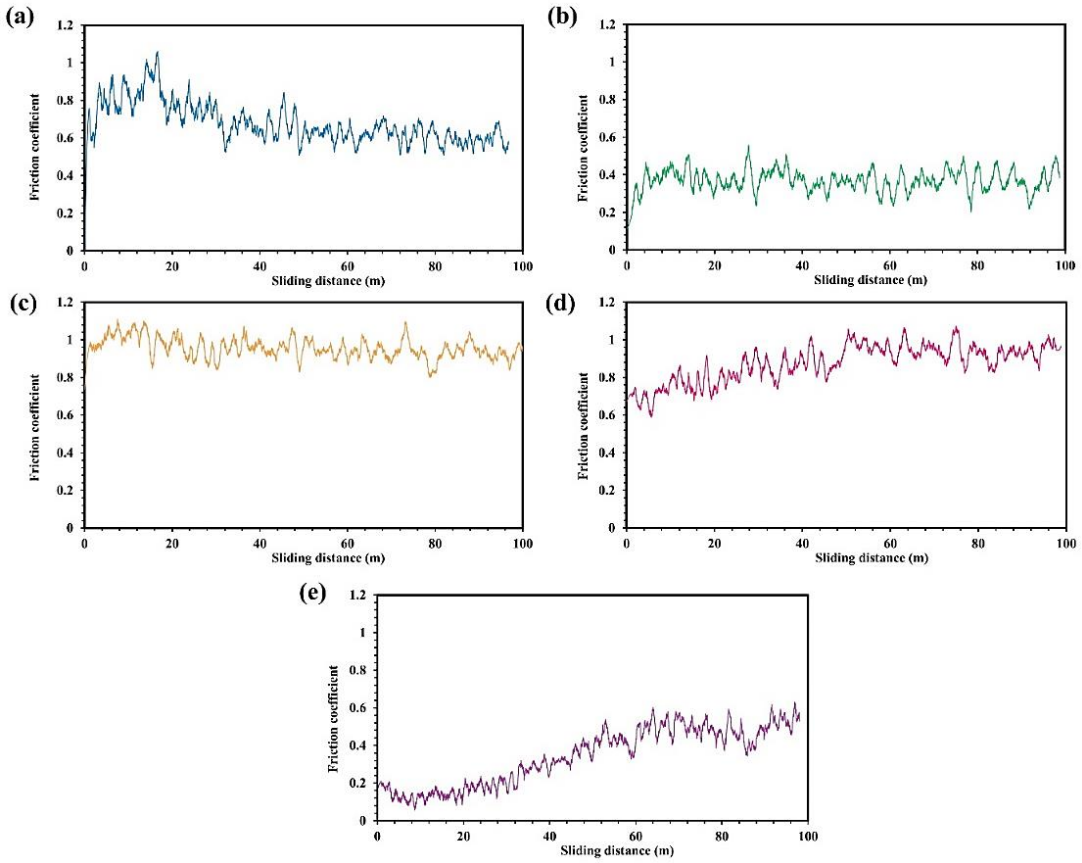

Figure 9. Changes in friction coefficient versus sliding distance of samples

The wear mechanism was determined by examining the wear tracks using FESEM images, as shown in Figure 11. It can be observed that the wear track of the A356 substrate is wider and deeper than those of the PEO-coated samples under identical wear conditions. The worn surface exhibits wide plowing marks and grooves parallel to the sliding direction, indicating the occurrence of an abrasive wear mechanism. The grooves observed on the A356 substrate originate from debris fragments generated during the plowing of the contacting surfaces. These detached particles penetrate the comparatively soft alloy surface, giving rise to three-body abrasive wear. The low hardness of the substrate promotes deeper indentation by the hard debris, which in turn facilitates the continuous detachment and re-entrainment of particles throughout sliding. Concurrently, evidence of crushing and tearing within the wear track indicates the simultaneous operation of an adhesive wear mechanism, likewise attributable to the substrate's limited hardness. This adhesive action results in the removal of material from the contact interface in the form of scale-like flakes. In contrast, the wear track of the unmodified oxide coating (T0) exhibits only shallow grooves and plowing marks, presenting a markedly smoother worn surface than the bare A356 substrate.

The superior wear performance of the unmodified oxide coating (T0) can be attributed to its high hardness and load-bearing capacity. Dark-colored spots present on the worn surface indicate the detachment of small particles from the oxide layer through mild adhesion, revealing the concurrent operation of abrasive and adhesive wear mechanisms. The wear track of sample T0.5 exhibits grooves accompanied by sheet-like fragments resulting from plastic deformation. Sample T1 displays a worn surface morphology similar to that of T0.5, although with less extensive plastic deformation. Consequently, the wear mechanism for both specimens is characterized by a combination of abrasive and adhesive wear. In contrast, the wear track of sample T2 is notably narrower and smoother than those of the other coatings. Its worn surface contains small scratches similar to those observed on T0, together with wear debris, indicating that abrasive wear is the dominant mechanism. The increased hardness of the oxide layer, combined with the presence of an optimal concentration of SiC nanoparticles that effectively reduces frictional shear stress, accounts for the limited degradation of the oxide layer in this sample (Nasiri Vatan et al., 2016; Sabatini et al., 2010; Sharifi et al., 2016; XIE et al., 2017).

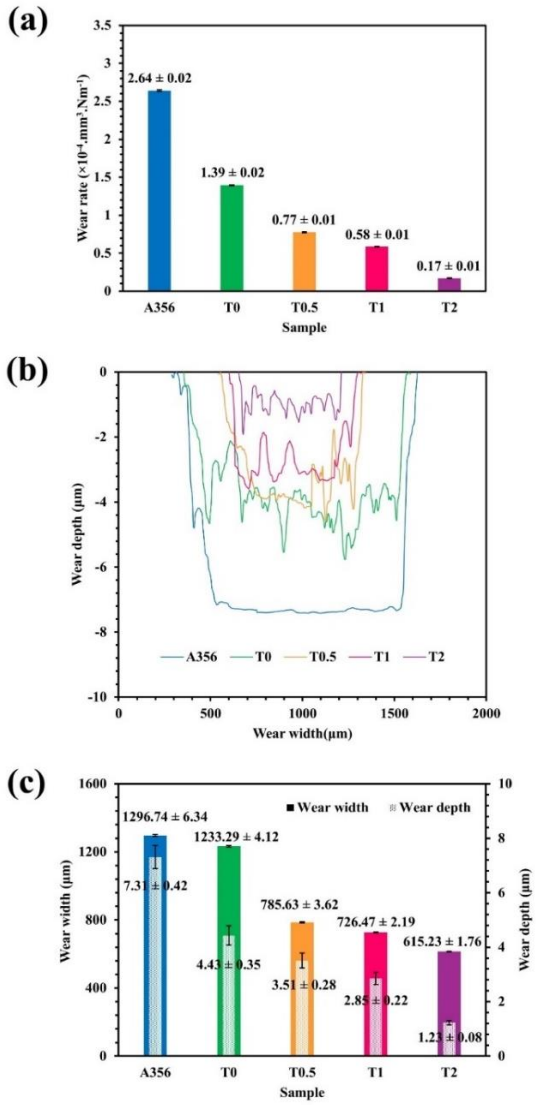

Figure 10. (a) changes in wear rates, (b) wear track profiles, and (c) wear track specifications of the samples

4. CONCLUSION

In this study, PEO coatings, both pure and incorporating different concentrations of SiC nanoparticles, were successfully grown on an A356 substrate, and their surface properties and tribological performance were investigated. The findings revealed that the PEO method can effectively produce homogeneous oxide coatings on A356 alloy. The oxide layer formed by this process exhibited a gamma-alumina crystal structure. The incorporation of SiC nanoparticles into the oxide coating increased the coating thickness and hardness while reducing its porosity and surface roughness. The formation of the oxide coating alone reduced the wear rate by a factor of approximately 1.9, whereas the incorporation of the highest concentration of SiC nanoparticles resulted in a substantially greater reduction, by a factor of approximately 15.5, relative to the bare alloy. The formation of a pure oxide coating reduced the friction coefficient throughout the sliding distance; however, the incorporation of SiC nanoparticles through the electrolyte at concentrations up to 1 $g \cdot L^{-1}$ led to an unfavorable increase in the friction coefficient. In contrast, the friction coefficient of the oxide coating formed in the electrolyte containing 2 $g \cdot L^{-1}$ SiC nanoparticles decreased significantly. This improvement was attributed to the presence of an appropriate concentration of SiC nanoparticles at the contact surfaces, which promoted a transition in the wear mechanism from sliding to rolling. This coating, which exhibited the best tribological performance by reducing both the friction coefficient and wear rate, could be considered a promising candidate for automotive components exposed to wear.

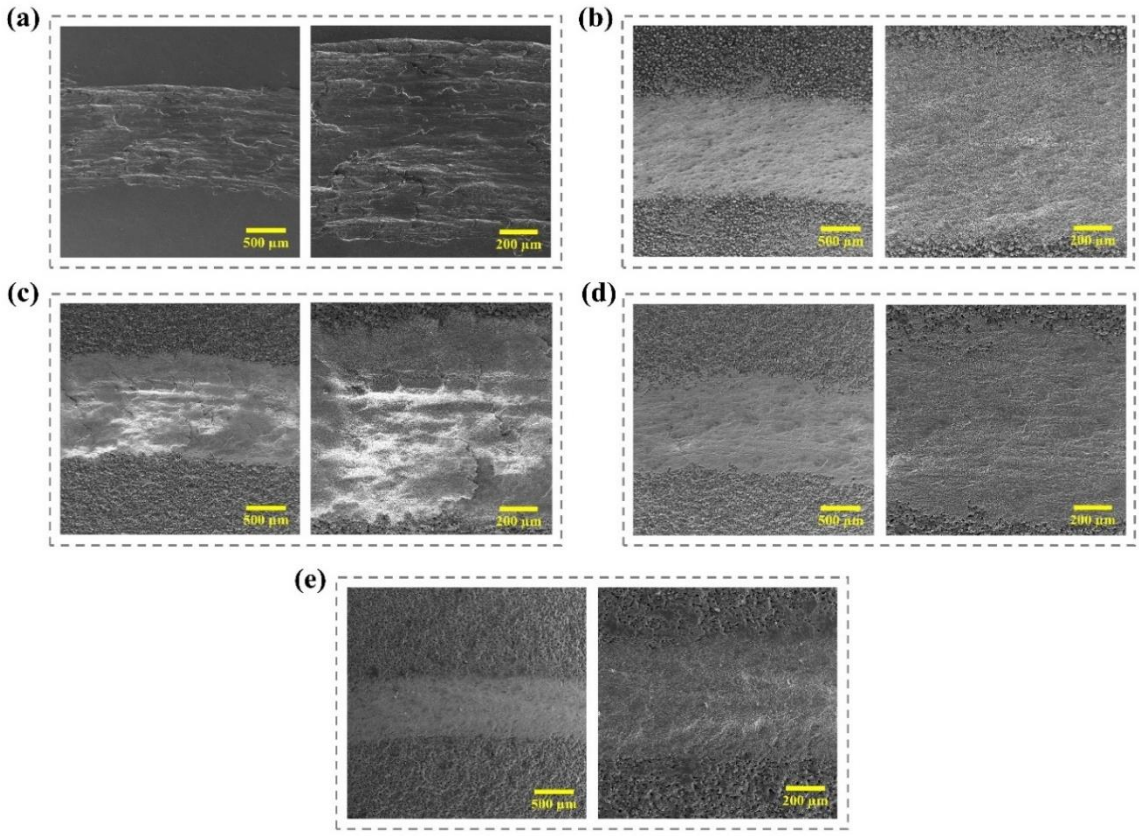

Figure 11. FESEM images from the wear track of the samples

ACKNOWLEDGEMENTS

This research has been supported via grant No.: 247383 by Materials and Energy Research Center, Karaj, Iran.

REFERENCES

1. Aljohani, T. A., Alawad, M. O., Elkatatny, S., Alateyah, A. I., Rubayan, M. T. B., Alhajji, M. A., Albeladi, M. I., Khoshnaw, F., & El-Garaihy, W. H. (2022). Electrochemical Behavior of SiC-Coated AA2014 Alloy through Plasma Electrolytic Oxidation. *Materials*, *15*(10), 3724. https://doi.org/10.3390/ma15103724

2. Alves, S. A., Fernández-Lopéz, P., Lopéz-Ortega, A., Fernández, X., Quintana, I., San-José, J. T., & Bayón, R. (2022). Enhanced tribological performance of cylinder liners made of cast aluminum alloy with high silicon content through plasma electrolytic oxidation. *Surface and Coatings Technology*, *433*, 128146. https://doi.org/10.1016/j.surfcoat.2022.128146

3. Dehnavi, V., Luan, B. L., Liu, X. Y., Shoesmith, D. W., & Rohani, S. (2015). Correlation between plasma electrolytic oxidation treatment stages and coating microstructure on aluminum under unipolar pulsed DC mode. *Surface and Coatings Technology*, *269*(1), 91–99. https://doi.org/10.1016/j.surfcoat.2014.11.007

4. Ebrahimi, S., Bordbar-Khiabani, A., & Yarmand, B. (2019). Enhanced optoelectronic performance of plasma electrolytic oxidized monocrystalline silicon using rGO incorporation. *Materials Letters*, *239*, 151–154. https://doi.org/10.1016/j.matlet.2018.12.086

5. Erfanifar, E., Aliofkhazraei, M., Nabavi, H. F., & Rouhaghdam, A. S. (2017). Growth kinetics and morphology of microarc oxidation coating on titanium. *Surface and Coatings Technology*, *315*, 567–576. https://doi.org/10.1016/j.surfcoat.2017.03.002

6. Fattah-alhosseini, A., Chaharmahali, R., & Babaei, K. (2020). Effect of particles addition to solution of plasma electrolytic oxidation (PEO) on the properties of PEO coatings formed on magnesium and its alloys: A review. *Journal of Magnesium and Alloys*, *8*(3), 799–818. https://doi.org/10.1016/j.jma.2020.05.001

7. Fernández-López, P., Alves, S. A., López-Ortega, A., San José-Lombera, J. T., & Bayón, R. (2021). High performance tribological coatings on a secondary cast Al–Si alloy generated by Plasma Electrolytic Oxidation. *Ceramics International*, *47*(22), 31238–31250. https://doi.org/10.1016/j.ceramint.2021.07.300

8. Fernández-López, P., Alves, S. A., San-Jose, J. T., Gutierrez-Berasategui, E., & Bayón, R. (2024). Plasma Electrolytic Oxidation (PEO) as a Promising Technology for the Development of High-Performance Coatings on Cast Al-Si Alloys: A Review. *Coatings*, *14*(2), 217. https://doi.org/10.3390/coatings14020217

9. Gulec, A. E., Gencer, Y., & Tarakci, M. (2015). The characterization of oxide based ceramic coating synthesized on Al-Si binary alloys by microarc oxidation. *Surface and Coatings Technology*, *269*(1), 100–107. https://doi.org/10.1016/j.surfcoat.2014.12.031

10. Hoseini, A., & Yarmand, B. (2020). Immobilization of Fe2O3/TiO2 photocatalyst on the metallic substrate via plasma electrolytic oxidation process: degradation efficiency. *Journal of*

Nanoparticle Research, *22*(11). https://doi.org/10.1007/s11051-020-05043-x

11. Hoseini, A., & Yarmand, B. (2023). Enhanced photocatalytic performance and photocorrosion stability of PEO-immobilized TiO2 photocatalyst using rGO/Fe2O3 sensitizers. *Surfaces and Interfaces*, *42*, 103424. https://doi.org/10.1016/j.surfin.2023.103424

12. Hoseini, A., & Yarmand, B. (2024). Photoelectrocatalytic and photocorrosion behavior of MoS2- and rGO-containing TiO2 bilayer photocatalyst immobilized by plasma electrolytic oxidation. *Journal of Alloys and Compounds*, *984*, 173976. https://doi.org/10.1016/j.jallcom.2024.173976

13. Hoseini, A., Yarmand, B., & Kolahi, A. (2021). Inhibitory effects of hematite nanoparticles on corrosion protection function of TiO2 coating prepared by plasma electrolytic oxidation. *Surface and Coatings Technology*, *409*, 126938. https://doi.org/10.1016/j.surfcoat.2021.126938

14. Hu, C. J., & Hsieh, M. H. (2014). Preparation of ceramic coatings on an Al-Si alloy by the incorporation of ZrO2 particles in microarc oxidation. *Surface and Coatings Technology*, *258*, 275–283. https://doi.org/10.1016/j.surfcoat.2014.09.012

15. Javidani, M., & Larouche, D. (2014). Application of cast Al-Si alloys in internal combustion engine components. *International Materials Reviews*, *59*(3), 132–158. https://doi.org/10.1179/1743280413Y.0000000027

16. Krishtal, M. M., Katsman, A. V., & Polunin, A. V. (2022). Effects of silica nanoparticles addition on formation of oxide layers on Al[sbnd]Si alloy by plasma electrolytic oxidation: The origin of stishovite under ambient conditions. *Surface and Coatings Technology*, *441*. https://doi.org/10.1016/j.surfcoat.2022.128556

17. Li, X., Nie, X., Wang, L., & Northwood, D. O. (2005). Corrosion protection properties of anodic oxide coatings on an Al-Si alloy. *Surface and Coatings Technology*, *200*(5–6), 1994–2000. https://doi.org/10.1016/j.surfcoat.2005.08.019

18. Lian, Y., Dai, X., & Zhang, J. (2020). Characterization of micro-arc oxidation coatings on Ti6Al4V with addition of SiC particle. *Materials Research Express*, *7*(1), 16438. https://doi.org/10.1088/2053-1591/ab6c9a

19. Lu, X., Mohedano, M., Blawert, C., Matykina, E., Arrabal, R., Kainer, K. U., & Zheludkevich, M. L. (2016). Plasma electrolytic oxidation coatings with particle additions – A review. *Surface and Coatings Technology*, *307*, 1165–1182. https://doi.org/10.1016/j.surfcoat.2016.08.055

20. Matykina, E., Berkani, A., Skeldon, P., & Thompson, G. E. (2007). Real-time imaging of coating growth during plasma electrolytic oxidation of titanium. *Electrochimica Acta*, *53*(4), 1987–1994. https://doi.org/10.1016/j.electacta.2007.08.074

21. Nasiri Vatan, H., Ebrahimi-Kahrizsangi, R., & Kasiri-Asgarani, M. (2016). Structural, tribological and electrochemical behavior of SiC nanocomposite oxide coatings fabricated by plasma electrolytic oxidation (PEO) on AZ31 magnesium alloy. *Journal of Alloys and Compounds*, *683*, 241–255. https://doi.org/10.1016/j.jallcom.2016.05.096

22. Polunin, A. V., Cheretaeva, A. O., Borgardt, E. D., Rastegaev, I. A., Krishtal, M. M., Katsman, A. V., & Yasnikov, I. S. (2021). Improvement of oxide layers formed by plasma electrolytic oxidation on cast Al–Si alloy by incorporating TiC nanoparticles. *Surface and Coatings Technology*, *423*, 127603. https://doi.org/10.1016/j.surfcoat.2021.127603

23. Rahimi, S., Yarmand, B., & Kolahi, A. (2020). Effects of process parameters on structure and corrosion behavior of PEO coated A356 alloy. *Surface Topography: Metrology and Properties*, *8*(4), 45020. https://doi.org/10.1088/2051-672X/abc736

24. Sabatini, G., Ceschini, L., Martini, C., Williams, J. A., & Hutchings, I. M. (2010). Improving sliding and abrasive wear behaviour of cast A356 and wrought AA7075 aluminium alloys by plasma electrolytic oxidation. *Materials and Design*, *31*(2), 816–828. https://doi.org/10.1016/j.matdes.2009.07.053

25. Sharifi, H., Aliofkhazraei, M., Darband, G. B., & Rouhaghdam, A. S. (2016). Characterization of PEO nanocomposite coatings on titanium formed in electrolyte containing atenolol. *Surface and Coatings Technology*, *304*, 438–449. https://doi.org/10.1016/j.surfcoat.2016.07.048

26. Wang, D. dong, Liu, X. tong, Wu, Y. kang, Han, H. ping, Yang, Z., Su, Y., Zhang, X. zhen, Wu, G. rui, & Shen, D. jiu. (2019). Evolution process of the plasma electrolytic oxidation (PEO) coating formed on aluminum in an alkaline sodium hexametaphosphate ((NaPO3)6) electrolyte. *Journal of Alloys and Compounds*, *798*, 129–143. https://doi.org/10.1016/j.jallcom.2019.05.253

27. XIE, H. jun, CHENG, Y. liang, LI, S. xian, CAO, J. hui, & CAO, L. (2017). Wear and corrosion resistant coatings on surface of cast A356 aluminum alloy by plasma electrolytic oxidation in moderately concentrated aluminate electrolytes. *Transactions of Nonferrous Metals Society of China (English Edition)*, *27*(2), 336–351. https://doi.org/10.1016/S1003-6326(17)60038-4

28. Yang, Y., & Liu, Y. (2010). Effects of Current Density on the Microstructure and the Corrosion Resistance of Alumina Coatings Embedded with SiC Nano-particles Produced by Micro-arc Oxidation. *Journal of Materials Science and Technology*, *26*(11), 1016–1020. https://doi.org/10.1016/S1005-0302(10)60167-3

29. Yerokhin, A., & Khan, R. H. U. (2010). Anodising of light alloys. In *Surface Engineering of Light Alloys: Aluminium, Magnesium and Titanium Alloys* (pp. 83–109). Elsevier. https://doi.org/10.1533/9781845699451.2.83

30. Yerokhin, A. L., Nie, X., Leyland, A., & Matthews, A. (2000). Characterisation of oxide films produced by plasma electrolytic oxidation of a Ti-6Al-4V alloy. *Surface and Coatings Technology*, *130*(2–3), 195–206. https://doi.org/10.1016/S0257-8972(00)00719-2

31. Yerokhin, A. L., Nie, X., Leyland, A., Matthews, A., & Dowey, S. J. (1999). Plasma electrolysis for surface engineering. *Surface and Coatings Technology*, *122*(2–3), 73–93. https://doi.org/10.1016/S0257-8972(99)00441-7

32. Yu, L., Cao, J., & Cheng, Y. (2015). An improvement of the wear and corrosion resistances of AZ31 magnesium alloy by plasma electrolytic oxidation in a silicate-hexametaphosphate electrolyte with the suspension of SiC nanoparticles. *Surface and Coatings Technology*, *276*, 266–278. https://doi.org/10.1016/j.surfcoat.2015.07.014

33. 33. Zhang, W., & Xu, J. (2022). Advanced lightweight materials for Automobiles: A review. *Materials and Design*, *221*, 110994. https://doi.org/10.1016/j.matdes.2022.110994